Numerical Heat Transfer, Part A: Applications: An International Journal of Computation and Methodology
Publication details, including instructions for authors and subscription information:
http://www.tandfonline.com/loi/unht20

EFFECTS OF ASPECT RATIO ON VORTEX FLOW PATTERNS IN MIXED CONVECTION OF AIR THROUGH A BOTTOM-HEATED HORIZONTAL RECTANGULAR DUCT

C. H. Yu [a] & T. F. Lin [a]
[a] Department of Mechanical Engineering , National Chiao Tung University , Hsinchu, Taiwan
Published online: 23 Mar 2007.

To cite this article: C. H. Yu & T. F. Lin (1997) EFFECTS OF ASPECT RATIO ON VORTEX FLOW PATTERNS IN MIXED CONVECTION OF AIR THROUGH A BOTTOM-HEATED HORIZONTAL RECTANGULAR DUCT, Numerical Heat Transfer, Part A: Applications: An International Journal of Computation and Methodology, 31:7, 745-764

To link to this article: http://dx.doi.org/10.1080/10407789708914062

EFFECTS OF ASPECT RATIO ON VORTEX FLOW PATTERNS IN MIXED CONVECTION OF AIR THROUGH A BOTTOM-HEATED HORIZONTAL RECTANGULAR DUCT

C. H. Yu and T. F. Lin
Department of Mechanical Engineering, National Chiao Tung University, Hsinchu, Taiwan

Buoyancy-induced vortex flow structures and the associated heat transfer were numerically investigated in a mixed convective air flow in a bottom-heated horizontal rectangular duct of different aspect ratios. The unsteady three-dimensional Navier-Stokes and energy equations were directly solved by a higher order upwind finite difference scheme. Results were presented in particular for Reynolds numbers ranging from 5 to 15, Rayleigh numbers up to 9000, and aspect ratios from 4 to 12. The predicted results clearly show significant differences in vortex structures induced in ducts with small and large aspect ratios. For an aspect ratio less than 6 the transverse vortex rolls are periodically generated in the duct entry and gradually transform into longitudinal rolls when moving downstream. The resulting vortex flow eventually evolves to a time periodic state with the upstream and downstream portions of the duct dominated by the transverse rolls and longitudinal rolls, respectively. For a large aspect ratio ($A > 9$) the transverse rolls prevail in the duct core, with two to three longitudinal rolls existing near each sidewall. The flow oscillation in the region dominated by the transverse rolls is much higher than that dominated by the longitudinal rolls. At high Ra the flow becomes chaotic in time, and the duct is filled with unstable irregular vortex rolls.

INTRODUCTION

The buoyancy-driven secondary flow structure and the associated heat transfer in a mixed convective flow through a horizontal rectangular duct are known to be relatively sensitive to the geometry of the duct characterized by its aspect ratio (A), in addition to the Prandtl (Pr), Reynolds (Re), and Rayleigh (Ra) numbers. In a duct of low aspect ratio ($A \leqslant 4$) the flow is dominated by the longitudinal vortex rolls due to the important viscous damping effects of the sidewalls. In a duct of large aspect ratio ($A \geqslant 8$) with distant sidewalls the vortex flow can be in the form of longitudinal or transverse rolls or a mixture of both, depending on Re. However, no systematic study has been carried out in the literature to delineate the effects of the duct aspect ratio on the induced flow and thermal characteristics. This investigation of the aspect ratio effects on the detailed flow and thermal structural

Received 20 March 1996; accepted 11 December 1996.
The financial support of this study by the engineering division of the National Science Council of Taiwan, R. O. C., through Contract NSC82-0404-E0009-141 is greatly appreciated.
Professor Tsing-Fa Lin, Department of Mechanical Engineering, National Chiao Tung University, 1001 Ta Hsueh Road, Hsinchu, Taiwan 30049. E-mail: u8414823@cc.nctu.edu.tw

Numerical Heat Transfer, Part A, 31:745–764, 1997

1040–7782/97 $12.00 + .00

NOMENCLATURE

A	aspect ratio ($= b/d$)	t	dimensionless time
b	duct width	T_c	temperature of the cold wall
Bi	sidewall heat loss coefficient ($= h_a d/k$)	T_h	temperature of the hot wall
d	duct height	u, v, w	dimensionless velocity components in X, Y, Z directions ($= U/\overline{W}, V/\overline{W}, W/\overline{W}$)
g	acceleration due to gravity		
Gr	Grashof number $[= g\beta(T_h - T_c)d^3/\nu^2]$	U, V, W	velocity components in x, y, z directions
h_a	average heat transfer coefficient from the sidewalls to the ambient	$\overline{W}$	mean velocity of the forced flow
		x, y, z	dimensionless coordinates ($= X/d, Y/d, Z/d$)
k	thermal conductivity of air in the duct	X, Y, Z	dimensional coordinates
L	dimensionless heating section length	α	thermal diffusivity
		β	volumetric coefficient of thermal expansion
L_a	dimensionless adiabatic section length in the upstream	θ	nondimensional temperature $[= (T - T_c)/(T_h - T_c)]$
p, P_m	dimensionless and dimensional dynamic pressures $[p = P_m/(\rho\alpha^2/L^2)]$	ν	kinematic viscosity
Pr	Prandtl number of fluid ($= \nu/\alpha$)		
Ra	Rayleigh number $[g\beta(T_h - T_c)d^3/\alpha\nu]$	**Subscripts**	
Re	Reynolds number ($= \overline{W}d/\nu$)	i, j, k	node indices

changes is particularly important in the thermal and flow design of the chemical vapor deposition (CVD) processes for growing thin solid films for the semiconductor industries. In CVD processes the Re of gas flow is relatively low ($Re \leqslant 50$) and the Ra is rather high ($Ra > 5000$). This high buoyancy-to-inertia ratio results in unstable vortex flow and heat transfer in CVD reactors, and the deposition rate is spatially nonuniform and time dependent on isothermal substrates. Thus the grown film is nonuniform in thickness and contains defects. Moreover, the geometry of CVD reactors can be designed to reduce the unstable flow effects. The aspect ratio of the reactors can be even or odd or it can be a noninteger.

Considerable research has been carried out in the past to explore various characteristics of buoyancy-induced longitudinal vortex rolls in a rectangular duct flow from the stability analysis [1–4], experimental measurement [5–9], and numerical simulation [10–13] over wide ranges of Re and Ra covering steady and time-dependent mixed convection for high and low A. Nevertheless, very few results were obtained for a duct with an intermediate aspect ratio of $A = 5$–7. Moreover, no result was reported in the literature when A is an odd number. Detailed review of the literature on the longitudinal vortex flow was given in our previous study [13].

Even fewer works were conducted for transverse vortex flow at low Re. The existence of the transverse thermoconvective rolls was experimentally proven by Luijkx and Platten [14] in mixed convection of silicone oil ($Pr \approx 450$). The critical Ra for the onset of the transverse rolls was found to be a function of A and Pr. A flow regime map for nitrogen gas was proposed by Chiu et al. [15, 16] to locate the

boundaries among the flow with no roll and steady and unsteady vortex rolls. Ouazzani et al. [17, 18] provided a relation between the wave speed, mean velocity, and Ra for air flow with $1 < \mathrm{Re} < 9$ and $12{,}000 \leqslant \mathrm{Ra} \leqslant 20{,}000$. They also refined the flow regime map to include the transverse rolls.

To explore the effects of the aspect ratio on the vortex flow structure, a time-accurate three-dimensional numerical simulation was conducted in the present study for an air flow through a bottom-heated rectangular duct. Attention was focused on the effects of the aspect ratio on the changes in the longitudinal, transverse, and mixed roll structures.

MATHEMATICAL MODELING

Considered in the present numerical simulation is a mixed convective air flow with a mean velocity $\overline{W}$ in a differentially heated horizontal rectangular duct, as schematically shown in Figure 1 along with the chosen coordinates. Initially, at time $t < 0$ the flow in the duct is hydrodynamically fully developed and at a uniform temperature T_c, which is the same as the ambient temperature. At time $t = 0$ the bottom plate temperature is suddenly raised to a higher uniform value T_h and the top plate is kept at the initial temperature T_c over a finite portion of the

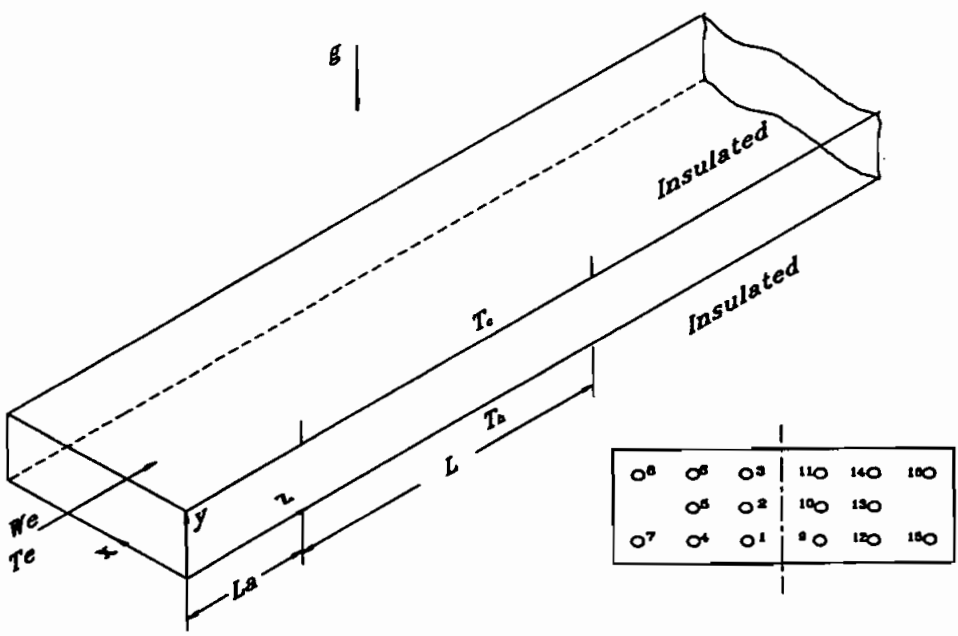

Figure 1. Schematic of the physical system and the detection points at a cross section. The x and y coordinates at various points are as follows: point 1, $(A/2 + 5\xi, 3\eta)$; point 2, $(A/2 + 5\xi, 0.5)$; point 3, $(A/2 + 5\xi, 1 - 3\eta)$; point 4, $(3A/4, 3\eta)$; point 5, $(3A/4, 0.5)$; point 6, $(3A/4, 1 - 3\eta)$; point 7, $(A - 5\xi, 3\eta)$; point 8, $(A - 5\xi, 0.5)$; point 9, $(A/2 - 5\xi, 3\eta)$; point 10, $(A/2 - 5\xi, 0.5)$; point 11, $(A/2 - 5\xi, 1 - 3\eta)$; point 12, $(A/4, 3\eta)$; point 13, $(A/4, 0.5)$; point 14, $(A/4, 1 - 3\eta)$; point 15, $(5\xi, 1 - 3\eta)$; point 16, $(5\xi, 0.5)$, where $\xi = A/mx$, $\eta = 1/my$, and A is aspect ratio.

duct $L_a \leqslant z \leqslant L_a + L$, and both are maintained at these levels thereafter. Heat loss from the duct flow through the sidewalls is also considered. When length, time, velocity, and temperature are scaled with the duct height d, mean convection time $d/\overline{W}$, mean velocity $\overline{W}$, and temperature difference ΔT $(= T_h - T_c)$, respectively, basic nondimensional equations describing the temporal and spatial evolution of the buoyancy-induced vortex flow of a Boussinesq fluid studied here are

$$\frac{\partial u}{\partial x} + \frac{\partial v}{\partial y} + \frac{\partial w}{\partial z} = 0 \tag{1}$$

$$\frac{\partial u}{\partial t} + u\frac{\partial u}{\partial x} + v\frac{\partial u}{\partial y} + w\frac{\partial u}{\partial z} = -\frac{\partial p}{\partial x} + \frac{1}{\mathrm{Re}}\left(\frac{\partial^2 u}{\partial x^2} + \frac{\partial^2 u}{\partial y^2} + \frac{\partial^2 u}{\partial z^2}\right) \tag{2}$$

$$\frac{\partial v}{\partial t} + u\frac{\partial v}{\partial x} + v\frac{\partial v}{\partial y} + w\frac{\partial v}{\partial z} = -\frac{\partial p}{\partial y} + \frac{1}{\mathrm{Re}}\left(\frac{\partial^2 v}{\partial x^2} + \frac{\partial^2 v}{\partial y^2} + \frac{\partial^2 v}{\partial z^2}\right) + \frac{\mathrm{Gr}}{\mathrm{Re}^2}\theta \tag{3}$$

$$\frac{\partial w}{\partial t} + u\frac{\partial w}{\partial x} + v\frac{\partial w}{\partial y} + w\frac{\partial w}{\partial z} = -\frac{\partial p}{\partial z} + \frac{1}{\mathrm{Re}}\left(\frac{\partial^2 w}{\partial x^2} + \frac{\partial^2 w}{\partial y^2} + \frac{\partial^2 w}{\partial z^2}\right) \tag{4}$$

$$\frac{\partial \theta}{\partial t} + u\frac{\partial \theta}{\partial x} + v\frac{\partial \theta}{\partial y} + w\frac{\partial \theta}{\partial z} = \frac{1}{\mathrm{Re\,Pr}}\left(\frac{\partial^2 \theta}{\partial x^2} + \frac{\partial^2 \theta}{\partial y^2} + \frac{\partial^2 \theta}{\partial z^2}\right) \tag{5}$$

which are subject to the following initial and boundary conditions:

$t < 0 \quad u = v = 0 \qquad w = w_{fd} \qquad \theta = 0$

$t \geqslant 0$

$$\begin{array}{llll}
x = 0 & & u = v = w = 0 & \dfrac{\partial \theta}{\partial x} - \mathrm{Bi}\,\theta = 0 \\
x = A & & u = v = w = 0 & \dfrac{\partial \theta}{\partial x} + \mathrm{Bi}\,\theta = 0 \\
y = 0 & L_a \leqslant z \leqslant L + L_a & u = v = w = 0 & \theta = 1 \\
y = 0 & 0 \leqslant z < L_a \qquad z > L + L_a & u = v = w = 0 & \dfrac{\partial \theta}{\partial y} = 0 \\
y = 1 & L_a \leqslant z \leqslant L + L_a & u = v = w = 0 & \theta = 0 \\
y = 1 & 0 \leqslant z < L_a \qquad z > L + L_a & u = v = w = 0 & \dfrac{\partial \theta}{\partial y} = 0 \\
z = 0 & & u = v = 0 \qquad w = w_{fd} & \theta = 0 \\
z \to \infty & & \dfrac{\partial u}{\partial z} = \dfrac{\partial v}{\partial z} = \dfrac{\partial w}{\partial z} = \dfrac{\partial \theta}{\partial z} = 0 &
\end{array} \tag{6}$$

where the inlet velocity w_{fd} is assumed as fully developed,

$$w_{fd} = \left(\frac{m+1}{m}\right)\left(\frac{n+1}{n}\right)\left[1 - (|2y-1|)^n\right]\left[1 - \left(\left|\frac{2x}{A} - 1\right|\right)^m\right] \tag{7}$$

with the values of the constants m and n depending on the aspect ratio A [19]. In treating the convective heat loss from the sidewalls to the ambient, the correlation for the average natural convection heat transfer coefficient from a vertical plate is used [20], so that

$$\mathrm{Bi} = 0.68 + \frac{0.67\,\mathrm{Ra}^{1/4}}{\left[1 + (0.492/\mathrm{Pr})^{9/16}\right]^{4/9}} \tag{8}$$

The nondimensional groups in the above formulation are defined as

$$\mathrm{Re} = \frac{\bar{W}d}{\nu} \qquad \mathrm{Pr} = \frac{\nu}{\alpha} \qquad \mathrm{Gr} = \frac{g\beta(T_h - T_c)d^3}{\nu^2}$$
$$A = \frac{b}{d} \qquad \mathrm{Bi} = \frac{h_a d}{k} \tag{9}$$

To account for the upstream diffusion at a low-Re flow, an upstream insulated section of length L_a was added to the heated section as shown in Figure 1. The selection of proper L_a will be discussed in the next section. The local Nusselt number (Nu), which signifies the heat transfer from the bottom-heated plate to the channel flow, is defined and evaluated as

$$\mathrm{Nu} \equiv \frac{hd}{k} = \frac{q''_w}{T_h - T_c}\frac{d}{k} = -\left.\frac{\partial\theta}{\partial y}\right|_{y=0} \tag{10}$$

where q''_w is local convective heat flux and k is the thermal conductivity of the fluid in the duct.

NUMERICAL SOLUTION

In view of the nonlinearity in the inertia terms, the basic equations were solved numerically. In particular, the projection method [21] was chosen to integrate the equations on a staggered grid system. This splitting (fractional step) method consists of two steps. First, a provisional velocity field was explicitly computed, ignoring the pressure gradient. Then it was corrected by including the pressure effect and by enforcing the mass conservation. The pressure distribution is obtained from solving the Poisson equation for pressure by the vectorized successive overrelaxation (SOR) method.

To enhance the numerical accuracy and stability, all the spatial derivatives were discretized by the fourth-order central differences [22] except the convective

terms, which were approximated by the third-order upwind difference proposed by Kawamura et al. [23]. For the nodes near the boundaries the usual second-order central difference was employed to facilitate the treatment of the boundary condition. This is not expected to significantly affect the accuracy of the solution, since the flow either is rather slow due to the no-slip condition near the solid boundaries or it changes slowly near the free boundaries. To allow for the possible presence of asymmetric flow with respect to the central vertical plane at $x = A/2$ for the time dependent flow induced at high Gr/Re^2, the computation domain includes both the left half and right half of the channel. Although the downstream boundary conditions were exactly specified at $z \to \infty$, only a finite unheated section is added in the downstream to facilitate the numerical analysis. Both this unheated section and the upstream insulated section must be long enough that the solution for the problem is independent of their sizes. Numerical tests indicated that the

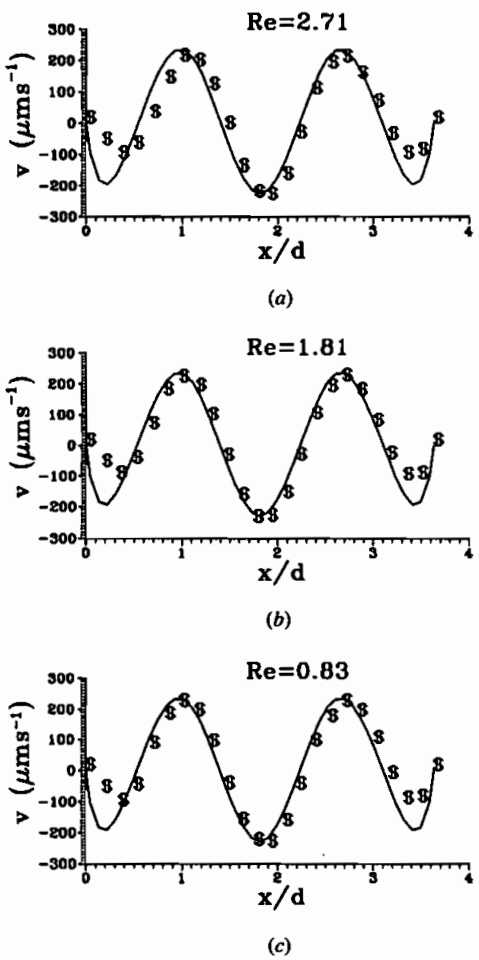

Figure 2. Comparison of the predicted velocity profile (*solid line*) at $y = 0.5$ at cross section $z = 15.66$ with the data of Ouazzani et al. [18] (\$\$\$) for Pr = 7, Ra = 2420, and $A = 3.63$.

suitable length for the upstream and downstream unheated sections is $0.2L$ and $0.47L$, respectively.

Time advancement may be done either implicitly or explicitly. The first-order Euler explicit scheme was employed here, since it was easy to implement. It has much lower computation cost per time step and requires much less computer memory allocation than any equivalent implicit implementation. We also found that the first-order scheme was sufficiently accurate to resolve the smallest physical timescale. The stability of the scheme is limited by requirement that the Courant number be less than unity [24]. To ensure the numerical convergence, the Courant number is set below 0.05 in the computation, which leads to

$$\Delta t < 0.05 \times \text{minimum}\left(\frac{\Delta x}{u_{\max}}, \frac{\Delta y}{v_{\max}}, \frac{\Delta z}{w_{\max}}\right) \tag{11}$$

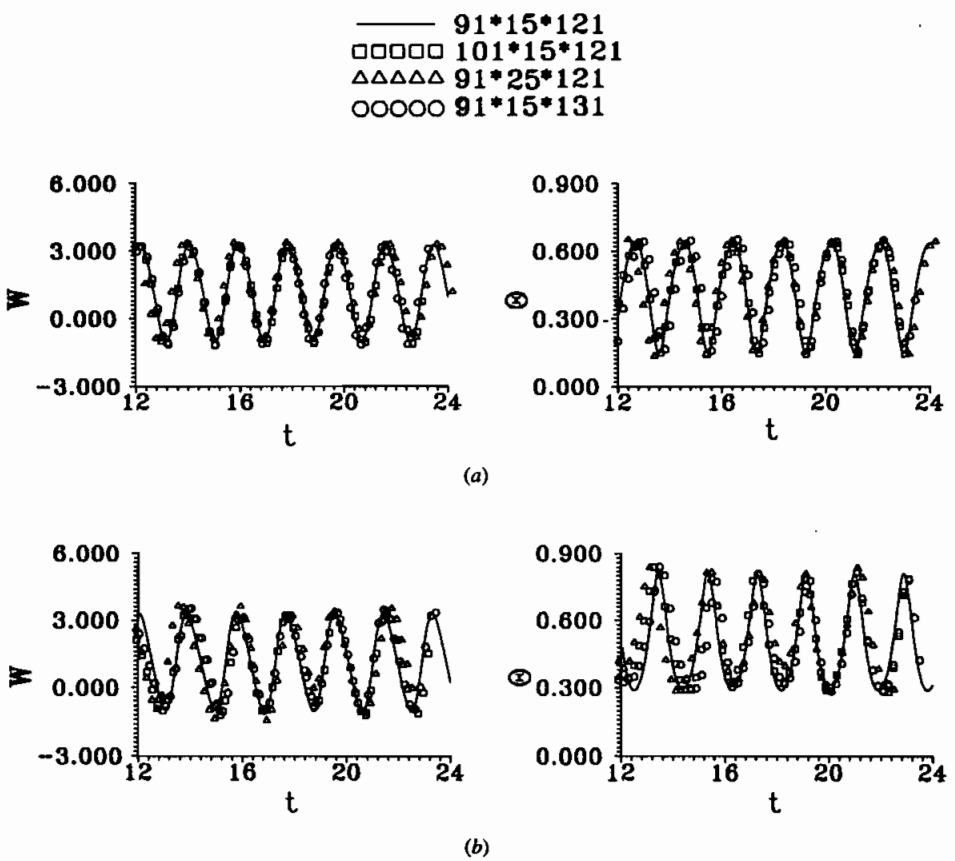

Figure 3. Comparison of the time oscillation of the axial velocity w and temperature θ at various locations computed by four different grids for Pr = 0.71, Re = 10, Ra = 5000, Bi = 5.01, A = 12, and L = 15. (*a*) Location (3.0, 0.77, 7.13); (*b*) location (3.0, 0.23, 14.57).

The sequence of numerical operation is as follows.

1. Explicitly calculate the provisional velocity.
2. Solve the pressure equation by the vectorized Gauss-Seidel method with SOR. Solution for the pressure is considered convergent when the mean relative pressure difference between two consecutive iterations is below 10^{-4}, that is

$$\sum_{i,j,k} \frac{\left|\left(p_{i,j,k}^{n+1}\right)^{m+1} - \left(p_{i,j,k}^{n+1}\right)^{m}\right|}{\left|\left(p_{i,j,k}^{n+1}\right)^{m+1}\right|} \Bigg/ (I \times J \times K) < 10^{-4} \qquad (12)$$

   where i, j, k are the indices of the nodes in the x, y, z directions respectively, m is the iteration number, and I, J, K are the total number of nodes in the x, y, z directions, respectively. This ensures the mass imbalance at each node to be less than 10^{-4} of the inlet mass flow rate.
3. Explicitly calculate the desired velocity and temperature fields at the new time step.

Procedures 1–3 were repeatedly applied from the initiation of the transient to a final steady state or to a statistical state when the flow was no longer steady at long time.

Stringent program tests were carried out in a previous study [25] to verify the proposed solution method. Very good agreement between the present predictions and published results in the literature was shown by comparing our predictions with the experimental data for the mixed convective vortex flow in a horizontal flat

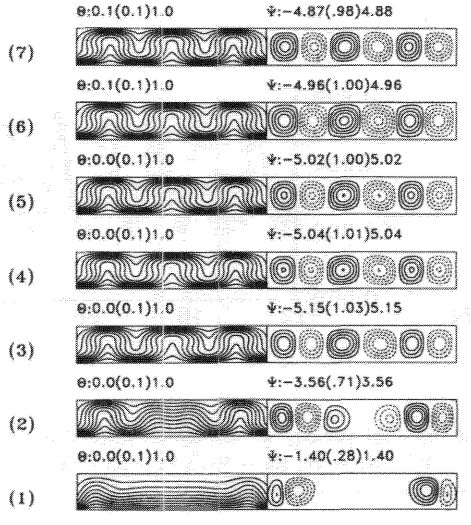

Figure 4. Steady isotherms and streamlines at selected cross sections for Pr = 0.71, Re = 15, Ra = 5000, and Bi = 5.01 at z = (1) 4.86, (2) 6.92, (3) 8.99, (4) 11.05, (5) 13.12, (6) 15.16, and (7) 17.25. In the streamlines the solid lines represent the counterclockwise recirculations, while the clockwise cells are indicated by the dashed lines.

duct [5, 15]. The comparison of our predicted velocity profile for a typical case with Pr = 7, Ra = 2420, and $A = 3.63$ with the experimental data of Ouazzani et al. [18] given in Figure 2 also shows good agreement. Finally, grid-independence tests were performed. Sample results from such tests indicate that the oscillation frequency of the flow, a very important characteristic of oscillatory flow, calculated from the $91 \times 15 \times 121$, $101 \times 15 \times 121$, $91 \times 25 \times 121$, and $91 \times 15 \times 131$ grids for a typical case with Re = 10, Ra = 5000, $A = 12$, $L = 15$, and Bi = 5, is 0.513, 0.513, 0.509, and 0.536, respectively. The differences between cases are all less than 4%. Moreover, the predicted time oscillations of the axial velocity w and temperature θ at large time at the locations (3.0, 0.77, 7.13) and (3.0, 0.23, 14.57) given in Figure 3 computed from the four different grid densities also show good agreement. Through these program tests, the adopted solution procedures are considered to be suitable for the present study. In the following computation the grid $91 \times 15 \times 121$ will be used.

RESULTS AND DISCUSSION

The above problem formulation clearly indicates that the flow to be investigated is governed by the Pr, Re, Ra, Bi, heating length L, and aspect ratio A. Systematic computation was carried out for air flow (Pr = 0.71) in a rectangular duct of aspect ratio varied from 4 to 12 with L fixed at 15. Re was varied from 5 to 15, and Ra from 4000 to 9000, covering various vortex flow patterns. Bi was varied from 4.77 to 5.69.

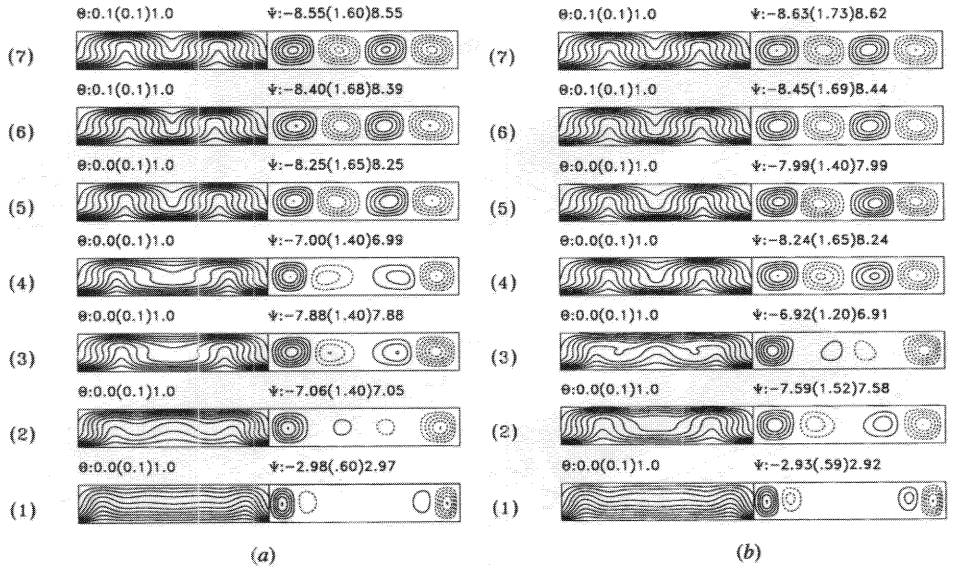

Figure 5. Isotherms and cross-plane streamlines for Re = 10, Ra = 5000, Bi = 5.01, and $A = 5$ at cross sections z = (1) 4.86, (2) 6.92, (3) 8.99, (4) 11.05, (5) 13.12, (6) 15.16, and (7) 17.25 at two time instants in a period: (*a*) $t + t_p/4$ and (*b*) $t + t_p 3/4$, where t_p is the time interval of a typical period ($t_p = 3.83$).

To illustrate the influences of Re and Ra on the flow structure in a duct with an intermediate aspect ratio, computation was carried out for various Re and Ra with A fixed at 5. The predicted results for the longitudinal vortex flow are examined first. Figure 4 shows the steady axial development of the longitudinal vortex rolls for a typical case with Re = 15 and Ra = 5000 by plotting the

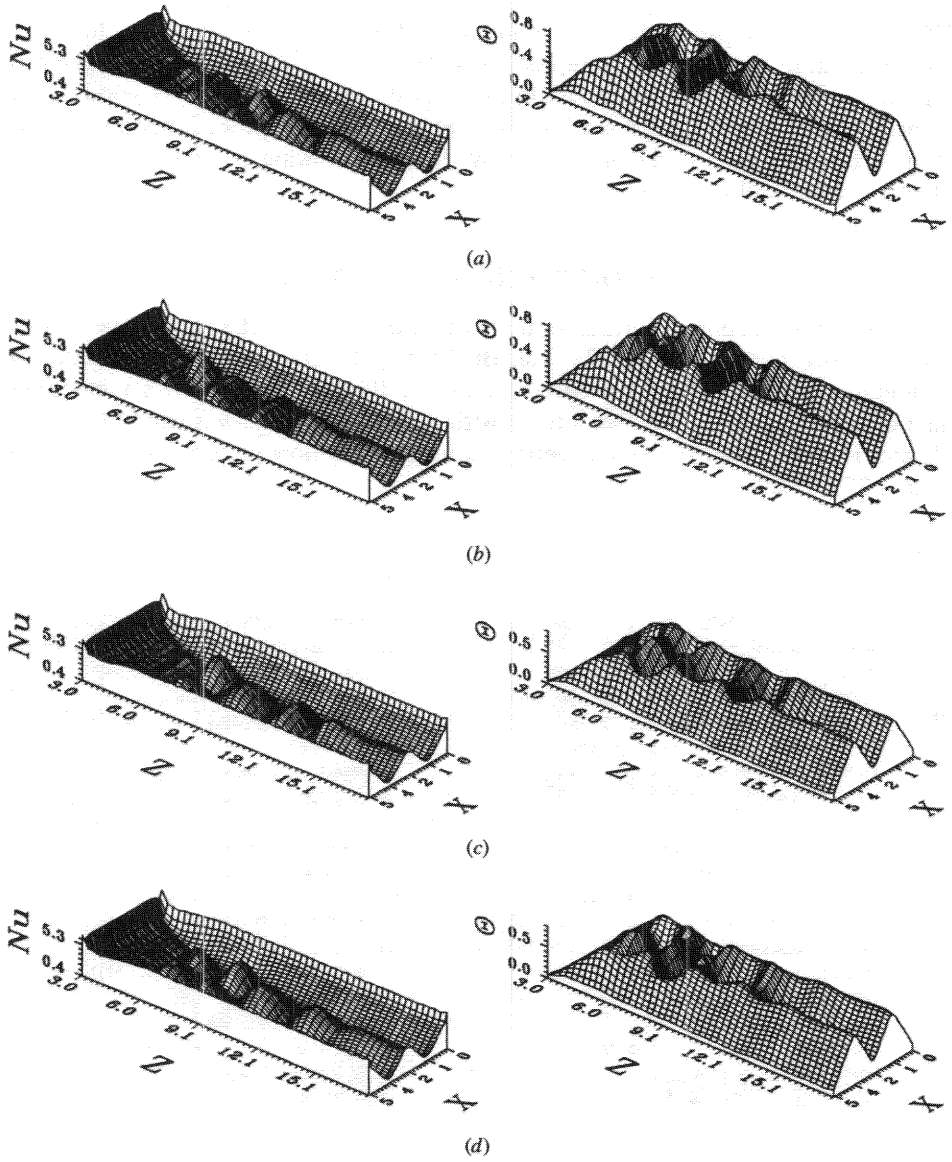

Figure 6. The local Nusselt number distributions on the bottom plate and the temperature distributions in the middle horizontal plane at $y = 0.5$ for Re = 10, Ra = 5000, Bi = 5.01, and $A = 5$ at four time instants (*a*) t, (*b*) $t + t_p/4$, (*c*) $t + 2t_p/4$, and (*d*) $t + 3t_p/4$.

cross-plane streamlines and isotherms at seven selected cross sections. The results indicate that in the entry region, two pairs of vortex rolls were first inducted near the sidewalls. As the flow moves downstream, more rolls are induced. At $z = 8.99$, three pairs of longitudinal vortex rolls occupy the cross section. Thus the roll number is larger than the aspect ratio, indicating the roll diameter is smaller than the duct height. In addition, a substantial change in the roll size during the axial development is noted in the entry region of the duct, $z < 8.2$. The flow down-

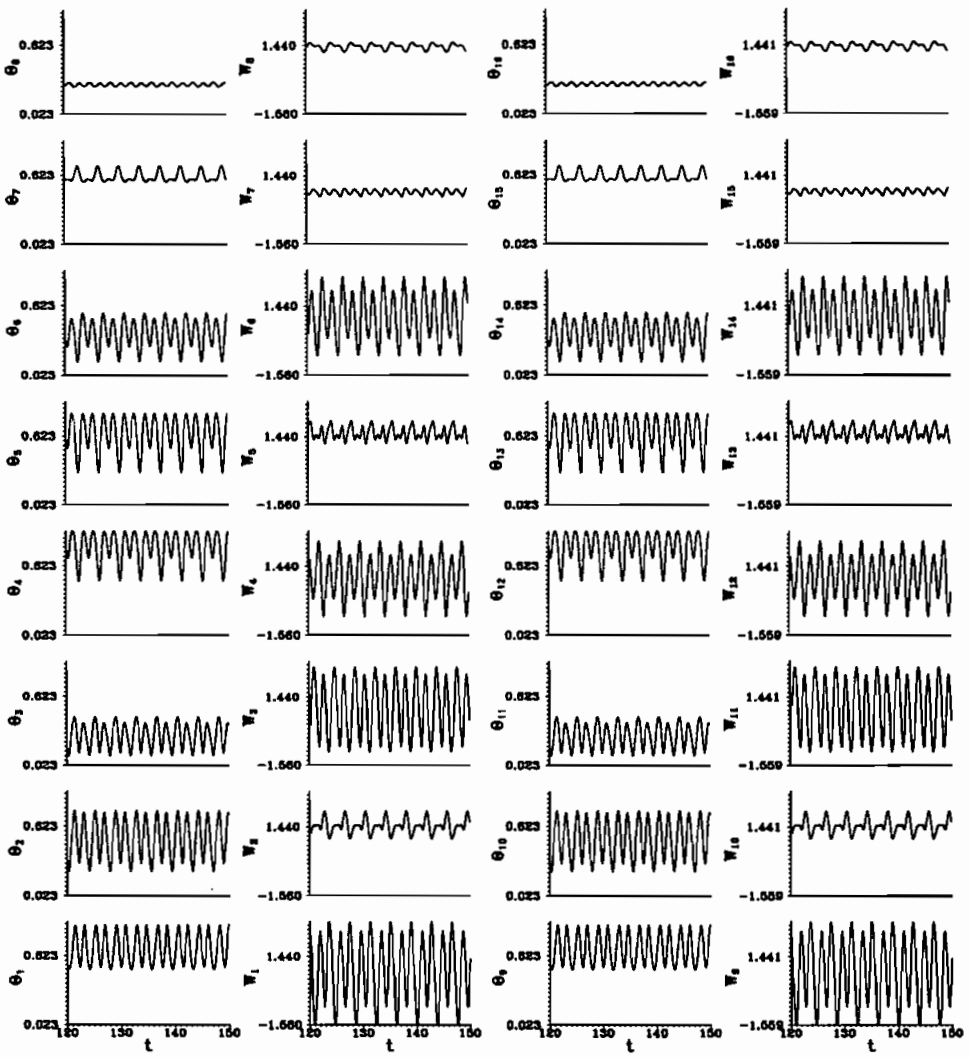

(*a*)

Figure 7. Time samples at selected detection points for w and θ for Re = 10, Ra = 5000, Bi = 5.01, and $A = 5$ at cross sections (*a*) $z = 7.13$ and (*b*) $z = 14.57$.

stream does not reach a fully developed state, since the duct is not long enough. The secondary flow intensity of the rolls increases significantly with the axial distance in the entry region. Note that the entire vortex flow is symmetric spanwise with respect to the vertical central plane at $x = A/2$.

When Re is reduced to 10 with Ra still fixed at 5000, the flow becomes time periodic. In addition, transverse rolls appear in the entry region of the heated section and move downstream during the initial transient. In the meantime, three pairs of the longitudinal rolls prevail in the exit part of the heated section. The

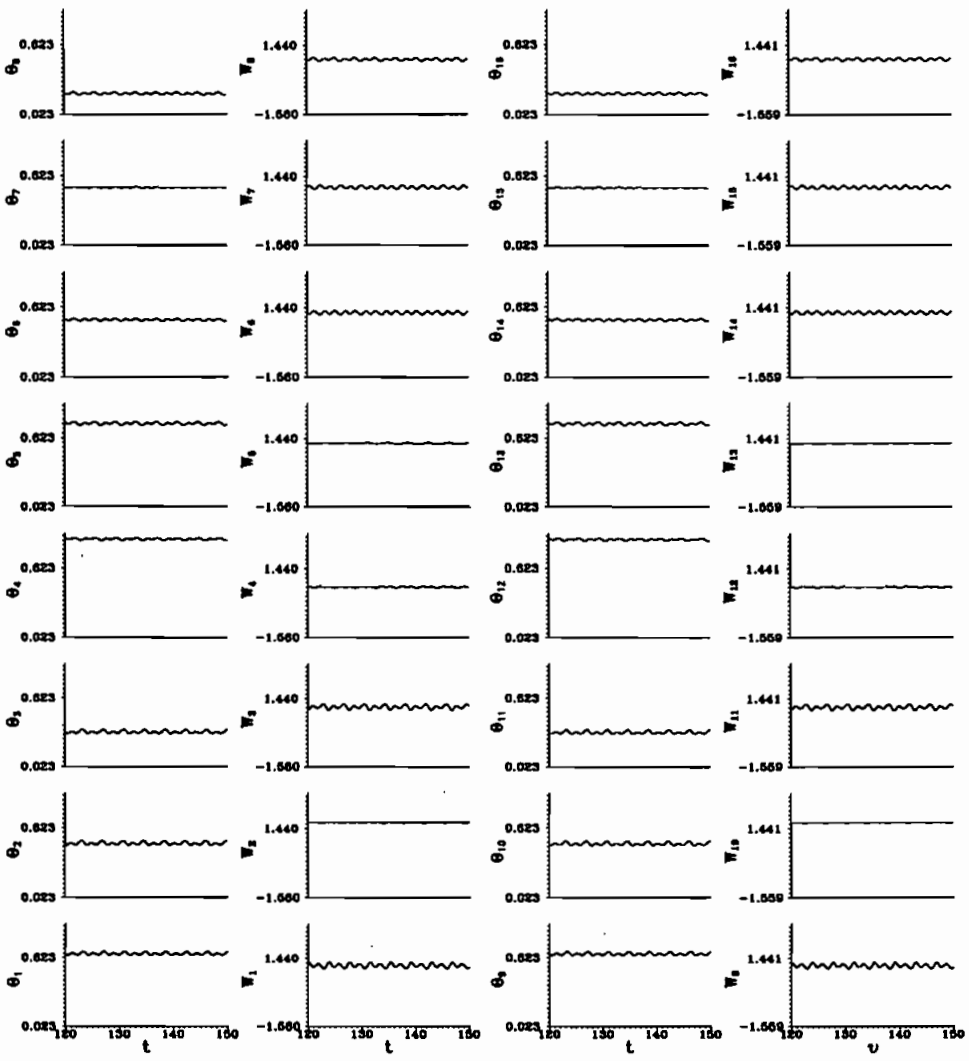

(*b*)

Figure 7. Time samples at selected detection points for w and θ for Re = 10, Ra = 5000, Bi = 5.01, and $A = 5$ at cross sections (*Continued*) (*b*) $z = 14.57$.

predicted vortex flow pattern when the flow has evolved to the time periodic state is displayed in Figures 5*a* and 5*b* at two time instants in a typical periodic cycle. It is important to note from the results that the flow structure varies from the transverse rolls in the entrance to the longitudinal rolls in the exit of the duct. This can also be clearly revealed from the local Nusselt number distributions on the bottom plate and the air temperature distributions in the horizontal plane at the midheight of the duct, as shown in Figure 6. More specifically, there are six to eight transverse rolls and four longitudinal rolls in the duct. Moreover, the interface between the longitudinal rolls and transverse rolls is not fixed at the same axial station but changes with time in the range $11.4 \leqslant z \leqslant 13.73$. To quantify the temporal characteristics in this interesting flow structure, time records of the air

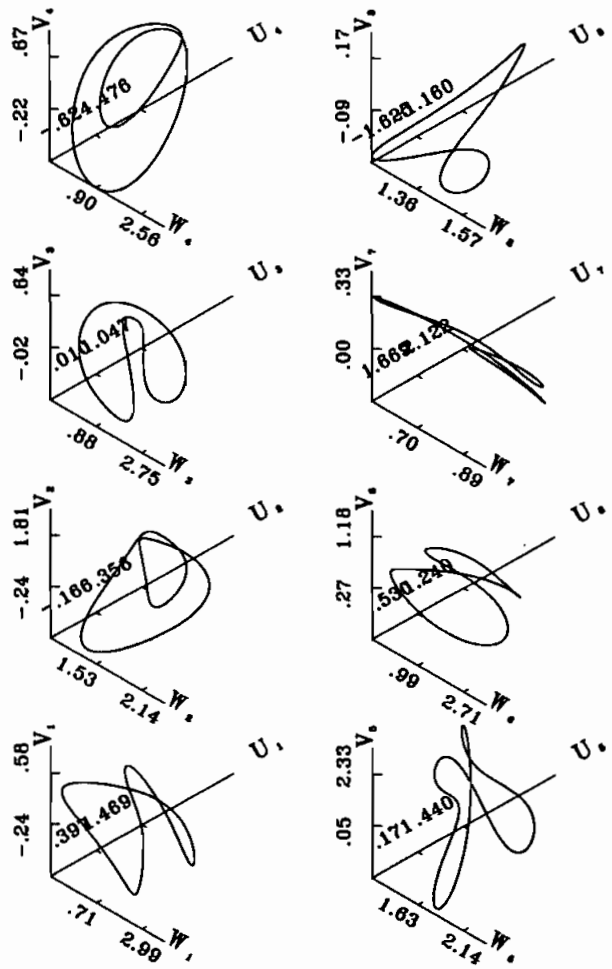

Figure 8. Phase space trajectories of u, v, and w at eight detection points for Re = 10, Ra = 5000, Bi = 5.01, and $A = 5$ at $z = 10.85$.

temperature and axial velocity at 16 selected locations specified in Figure 1 in two selected cross sections, located in the transverse and longitudinal roll regions, are given in Figures 7*a* and 7*b* for $t \geqslant 120$. The corresponding power spectrum densities for these records indicated that the flow in the entire duct oscillates at the same single fundamental frequency ($f_1 = 0.261$) and its harmonics. In addition, the flow oscillation is spanwise symmetric with respect to the vertical plane $x = A/2$ in the entire duct. It is noted that in the region of the transverse rolls, the amplitudes of the velocity oscillation near the top and bottom surfaces are much larger than that near the middle horizontal planes at $y = 0.5$ (Figure 7*a*) except in the region near the duct sides, where the viscous damping effect is large and the flow is in a small-amplitude oscillation. The flow oscillation in the region where the longitudinal rolls prevail is much weaker than that in the region dominated by the transverse rolls, as is evident from comparing the results in Figure 7*a* and 7*b*. To further illustrate the unsteady flow characteristics, the corresponding phase space trajectories of the velocity components u, v, and w for eight selected locations in the cross section $z = 10.85$ are given in Figure 8. Various limiting cycles are noted

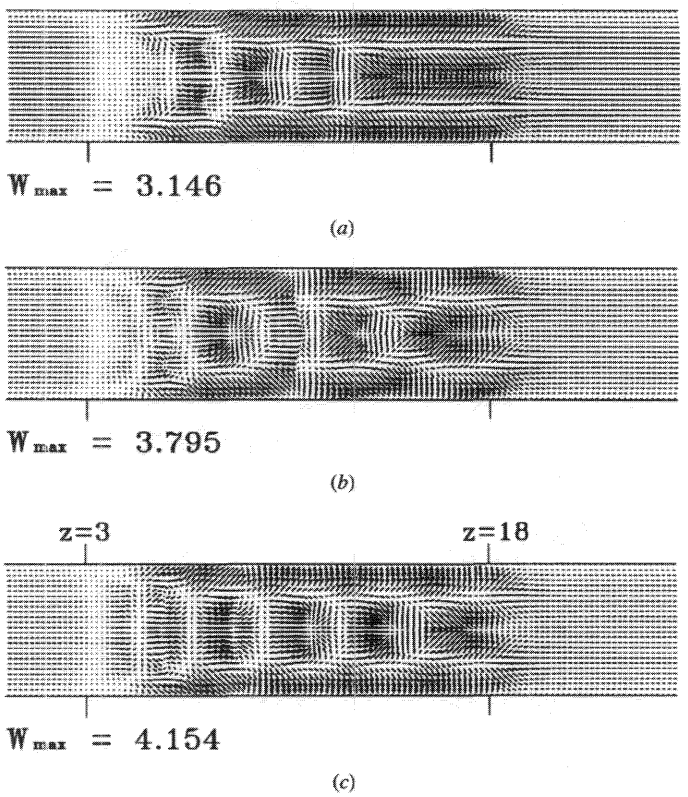

Figure 9. The instantaneous vector velocity maps in the horizontal plane at $y = 0.766$ for Re = 10, $A = 5$ and (*a*) Ra = 5000, Bi = 5.01 at $t = 120$; (*b*) Ra = 6000, Bi = 5.21 at $t = 90$; and (*c*) Ra = 7000, Bi = 5.39 at $t = 120$.

for all locations, signifying the flow being time periodic. Also note that the variations of u, v, and w with time are relatively different in a period. The predicted flow oscillation at high $\mathrm{Gr}/\mathrm{Re}^2$ was also reported in some experimental studies [17, 18].

Results for Re further lowered to 5 manifested that the longitudinal rolls develop far upstream and occupy almost the entire duct and that there exists only one pair of transverse rolls in the entrance of the duct. At $t > 60$ the flow evolves to a time periodic state. Note that this prevalence of longitudinal rolls for Re from 10 to 5 at $A = 5$ is contrary to that observed in a duct of large aspect ratio ($A \geqslant 10$). In wide ducts, transverse rolls become dominant at a lower Re ($\leqslant 15$).

To explore the effects of Ra on the vortex flow, a series of computations were conducted for Re fixed at 10 and Ra gradually increased. The results from these computations indicate that the vortex flow gradually evolves into a pattern dominated by the steady longitudinal rolls at large t for Re = 10 and Ra = 4000. As Ra is raised to the range between 5000 and 7000, the computed data show that after the initial transient the flow finally evolves to a time periodic state at a single

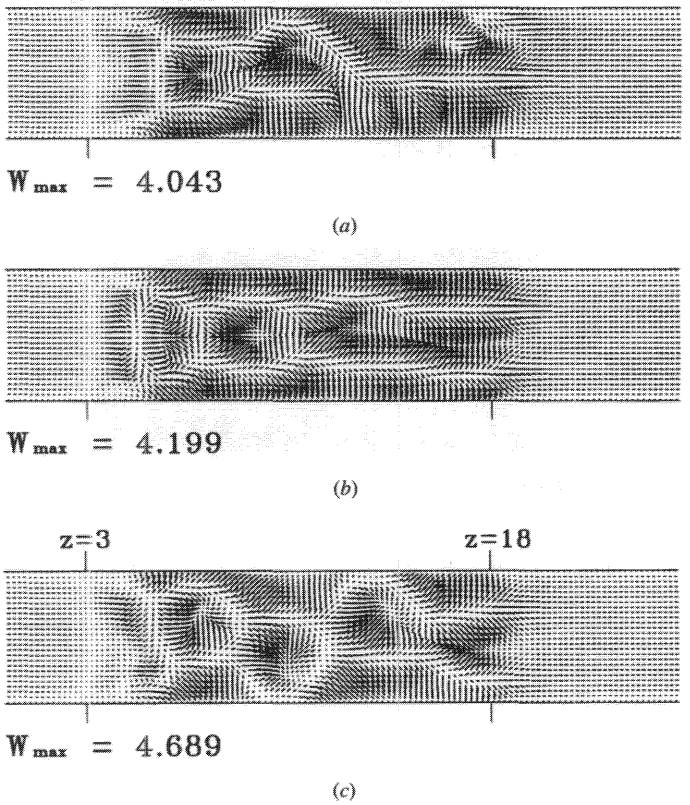

Figure 10. Vector velocity maps in the horizontal plane at $y = 0.766$ for Re = 10, Ra = 8000, Bi = 5.55, and $A = 5$ at three selected time instants: (*a*) $t = 114$, (*b*) $t = 124$, and (*c*) $t = 134$.

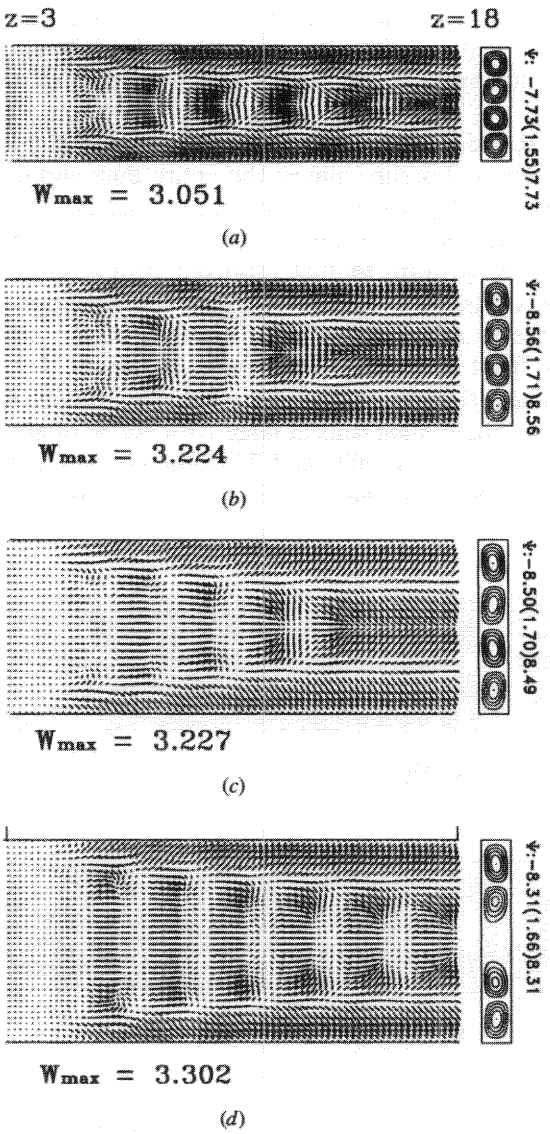

Figure 11. Vector velocity maps in the horizontal plane $y = 0.766$ and the streamlines at the cross section $z = 17.25$ for Re = 10, Ra = 5000, Bi = 5.01, and (*a*) $A = 4$, (*b*) $A = 5$, (*c*) $A = 6$, (*d*) $A = 7$.

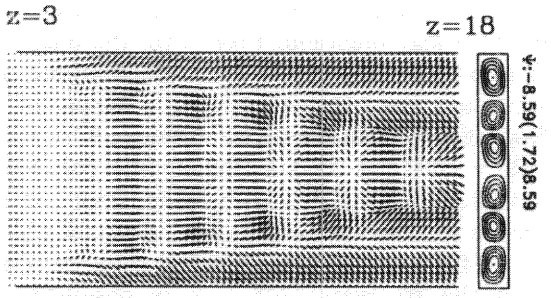

(*e*)

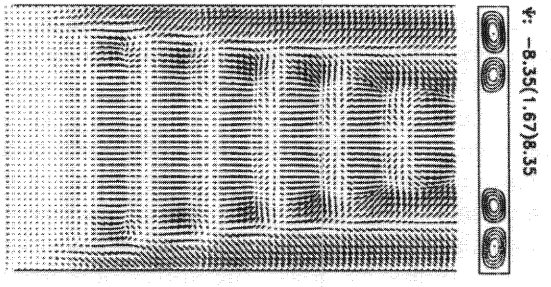

(*f*)

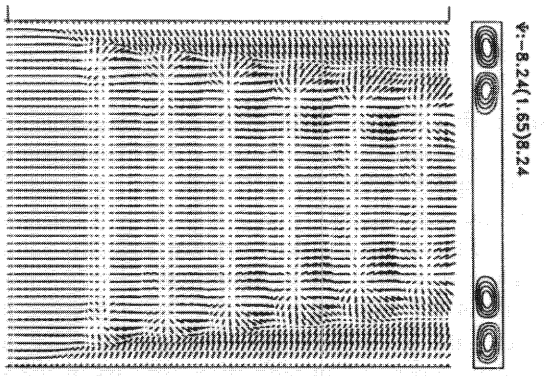

(*g*)

Figure 11. (*Continued*) Vector velocity maps in the horizontal plane $y = 0.766$ and the streamlines at the cross section $z = 17.25$ for Re = 10, Ra = 5000, Bi = 5.01, and (*e*) $A = 8$, (*f*) $A = 9$, and (*g*) $A = 12$.

fundamental frequency. The vortex flow is characterized by the transverse rolls in the entry half of the duct and longitudinal rolls near the duct sides and in the exit region. The flow is also spanwise symmetric. In addition, the transverse rolls can reach further downstream for a higher Ra. For instance, the planforms of the predicted vortex flows at $y = 0.766$ are shown in Figure 9 for Ra = 5000, 6000, and 7000. Note that at Ra = 6000 and 7000 the longitudinal rolls are distorted. Raising Ra still further to 8000 causes the flow to become chaotic in time. Results from this computation for the velocity vector maps in a horizontal plane at $y = 0.766$ are illustrated in Figure 10 for Re = 10, Ra = 8000 at three selected time instants. It is worth noting that the transverse roll is only observed in the duct entry. Downstream, however, the roll structure becomes rather irregular in time and space.

Results from another series of computations for Re = 10, Ra = 5000, and A varied from 4 to 12 are presented here to illustrate the effects of A on the changes in the vortex flow pattern. The predicted velocity vector maps in a horizontal plane at $y = 0.766$ are given in Figure 11 along with the cross-plane streamlines at $z = 17.25$. The results clearly suggest that for $A = 4$–6 a transverse roll structure is observed in the entry region of the heated section and downstream the longitudinal rolls prevail. It is worth noting that there exist two pairs of longitudinal rolls in the downstream region when $A < 7$. However, for $A \geqslant 7$ we observe two longitudinal rolls near each sidewall, and the extra space in the duct core provided by the larger A is dominated by the transverse rolls. The vortex flow in these ducts of high aspect ratio consists of the longitudinal rolls near the sidewalls and the moving transverse rolls in the core region. Thus the transverse rolls occupy larger regions for higher aspect ratios.

CONCLUDING REMARKS

Through a direct three-dimensional unsteady numerical simulation for mixed convection of air in a rectangular duct, various vortex flow structures were revealed for ducts of different aspect ratios. In particular, an even number of longitudinal rolls are induced for the aspect ratio $A = 5$ and Re = 15. Besides, at lower Re of 10 and 5, we observe an interesting flow pattern with the transverse rolls in the upstream portion of the duct and the longitudinal rolls downstream for $A = 4$–6. For a wider duct with $A \geqslant 7$ the mixed vortex flow structure is induced with the longitudinal rolls near the duct sides and transverse rolls in the core region. Moreover, substantial flow oscillation with time appears in the transverse rolls.

REFERENCES

1. Y. Mori and Y. Uchida, Forced Convective Heat Transfer Between Horizontal Flat Plates, *Int. J. Heat Mass Transfer*, vol. 9, pp. 803–817, 1996.
2. W. Nakayama, G. J. Hwang, and K. C. Cheng, Thermal Instability in Plane Poiseuille Flow, *J. Heat Transfer*, vol. 92, pp. 61–68, 1970.
3. G. J. Hwang and K. C. Cheng, Convective Instability in the Thermal Entrance Region of a Horizontal Parallel-Plate Channel Heated from Below, *J. Heat Transfer*, vol. 95, pp. 72–77, 1973.

4. F. S. Lee and G. J. Hwang, Transient Analysis on the Onset of Thermal Instability in the Thermal Entrance Region of a Horizontal Parallel Plate Channel, *J. Heat Transfer*, vol. 113, pp. 363–370, 1991.
5. S. Ostrach and Y. Kamotani, Heat Transfer Augmentation in Laminar Fully Developed Channel Flow by Means of Heating from Below, *J. Heat Transfer*, vol. 97, pp. 220–225, 1975.
6. Y. Kamotani and S. Ostrach, Effect of Thermal Instability on Thermally Developing Laminar Channel Flow, *J. Heat Transfer*, vol. 98, pp. 62–66, 1976.
7. D. G. Osborne and F. P. Incropera, Experimental Study of Mixed Convection Heat Transfer for Transitional and Turbulent Flow Between Horizontal Parallel Plates, *Int. J. Heat Mass Transfer*, vol. 28, pp. 1337–1344, 1985.
8. J. R. Maughan and F. P. Incropera, Regions of Heat Transfer Enhancement for Laminar Mixed Convection in a Parallel Plate Channel, *Int. J. Heat Mass Transfer*, vol. 33, pp. 555–570, 1990.
9. M. Y. Chang, C. H. Yu, and T. F. Lin, Changes of Longitudinal Vortex Roll Structures in a Mixed Convective Air Flow Through a Horizontal Plane Channel—An Experimental Study, *Int. J. Heat Mass Transfer*, vol. 40, pp. 343–367, 1997.
10. F. P. Incropera and J. A. Schutt, Numerical Simulation of Laminar Mixed Convection in the Entrance Region of a Horizontal Rectangular Duct, *Numer. Heat Transfer*, vol. 8, pp. 707–729, 1985.
11. H. V. Mahaney, F. P. Incropera, and S. Ramadhyani, Development of Laminar Mixed Convection Flow in a Horizontal Rectangular Duct with Uniform Bottom Heating, *Numer. Heat Transfer*, vol. 12, pp. 137–155, 1987.
12. H. V. Mahaney, F. P. Incropera, and S. Ramadhyani, Effect of Wall Heat Flux Distribution on Laminar Mixed Convection in the Entrance Region of a Horizontal Rectangular Duct, *Numer. Heat Transfer*, vol. 13, pp. 427–450, 1988.
13. C. C. Huang and T. F. Lin, Buoyancy-Induced Flow Transition in Mixed Convective Flow of Air Through a Bottom Heated Horizontal Rectangular Duct, *Int. J. Heat Mass Transfer*, vol. 37, no. 2, pp. 1235–1255, 1994.
14. J. M. Luijkx and J. K. Platten, On the Existence of Thermoconvective Rolls: Transverse to a Superimposed Mean Poiseuille Flow, *Int. J. Heat Mass Transfer*, vol. 24, pp. 1287–1291, 1981.
15. K. C. Chiu, J. Ouazzani, and F. Rosenberger, Mixed Convection Between Horizontal Plates, II: Fully Developed Flow, *Int. J. Heat Mass Transfer*, vol. 30, pp. 1655–1662, 1987.
16. K. C. Chiu and F. Rosenberger, Mixed Convection Between Horizontal Plates, I: Entrance Effects, *Int. J. Heat Mass Transfer*, vol. 30, pp. 1645–1654, 1987.
17. M. T. Ouazzani, J. P. Caltagirone, G. Meyer, and A. Mojtabi, Etude Numérique et Expérimentale de la Convection Mixte entre Deux Plans Horizontaux à Tempèratures Différentes, *Int. J. Heat Mass Transfer*, vol. 32, pp. 261–269, 1989.
18. M. T. Ouazzani, J. K. Platten, and A. Mojtabi, Etude Expérimentale de la Convection Mixte entre Deux Plans Horizontaux à Températures Différents, II, *Int. J. Heat Mass Transfer*, vol. 33, pp. 1417–1427, 1990.
19. R. K. Shah and A. L. London, *Laminar Flow Forced Convection in Ducts*, pp. 196–198, Academic, New York, 1978.
20. S. W. Churchill and H. H. S. Chu, Correlating Equations for Laminar and Turbulent Free Convection from a Vertical Plate, *Int. J. Heat Mass Transfer*, vol. 18, p. 1323, 1975.
21. R. Peyret and T. D. Taylor, *Computational Methods for Fluid Flow*, chap. 6, Springer-Verlag, New York, 1983.
22. C. Hirsch, *Numerical Computation of Internal and External Flow*, vol. I, pp. 176–179, John Wiley, New York, 1989.

23. T. Kawamura, H. Takami, and K. Kuwahara, New Higher-Order Upwind Scheme for Incompressible Navier-Stokes Equations, *9th ICNMFD*, vol. 10, pp. 285–291, 1985.
24. D. A. Anderson, J. C. Tannehill, and R. H. Pletcher, *Computational Fluid Mechanics and Heat Transfer*, pp. 71–77, Hemisphere, Washington, D.C., 1984.
25. C. H. Yu, M. Y. Chang, C. C. Huang, and T. F. Lin, Unsteady Vortex Roll Structures in a Mixed Convective Air Flow Through a Horizontal Plane Channel—A Numerical Study, *Int. J. Heat Mass Transfer*, vol. 40, pp. 505–518, 1997.